



Full Text View

Volume 32, Issue 7 (July 2002)

Journal of Physical Oceanography

Article: pp. 2113–2130 | [Abstract](#) | [PDF \(1.22M\)](#)

Observations of Boundary Mixing over the Continental Slope

J. N. Moum, D. R. Caldwell, J. D. Nash, and G. D. Gunderson

College of Oceanic and Atmospheric Sciences, Oregon State University, Corvallis, Oregon

(Manuscript received March 20, 2001, in final form December 7, 2001)

DOI: 10.1175/1520-0485(2002)032<2113:OOBMOT>2.0.CO;2

ABSTRACT

Observations of mixing over the continental slope using a towed body reveal a great lateral extent (several kilometers) of continuously turbulent fluid within a few hundred meters of the boundary at depth 1600 m. The largest turbulent dissipation rates were observed over a 5 km horizontal region near a slope critical to the M_2 internal tide. Over a submarine landslide perpendicular to the continental slope, enhanced mixing extended at least 600 m above the boundary, increasing toward the bottom. The resulting vertical divergence of the heat flux near the bottom implies that fluid there must be replenished.

Intermediate nepheloid layers detected optically contained fluid with θ - S properties distinct from their surroundings. It is suggested that intermediate nepheloid layers are interior signatures of the boundary layer detachment required by the near-bottom flux divergence.

1. Introduction

Awareness of the potential role of boundary mixing in modifying the waters of the ocean's interior arises from observations that

- interior diapycnal mixing is too weak to account for the observed vertical distributions of heat, salt, and density in the main thermocline in midocean ([Moum and Osborn 1986](#); [Gregg 1987](#); [Ledwell et al. 1993](#); [Toole et al. 1994](#); [Kunze and Sanford 1996](#)) and
- strong turbulence is generated in the vicinity of rough topography ([Toole et al. 1994](#); [Polzin et al. 1997](#); [Kunze and Toole 1997](#); [Polzin et al. 1996](#); [Lueck and Mudge 1997](#); [Ledwell et al. 2000](#)).

Table of Contents:

- [Introduction](#)
- [Methods](#)
- [Data](#)
- [Background](#)
- [Variability of \$\epsilon\$](#)
- [Vertical structure and](#)
- [Turbulent diffusivity](#)
- [Intermediate nepheloid](#)
- [Discussion](#)
- [Conclusions](#)
- [REFERENCES](#)
- [FIGURES](#)

Options:

- [Create Reference](#)
- [Email this Article](#)
- [Add to MyArchive](#)
- [Search AMS Glossary](#)

Search CrossRef for:

- [Articles Citing This Article](#)

Search Google Scholar for:

- [J. N. Moum](#)
- [D. R. Caldwell](#)
- [J. D. Nash](#)
- [G. D. Gunderson](#)

These observations lead to the idea that the apparent mixing of the interior takes place near boundaries, with water vertically mixed above rough topography carried to the interior along isopycnals ([Garrett 1993](#)). The competitiveness of this process has not been established; that is, we do not know whether such mixing occurs with sufficient intensity and frequency at the boundary and whether the movement of mixed fluid along isopycnals is fast enough to accomplish the observed alteration of the vertical profiles in mid ocean. Several specific mechanisms have been suggested to be responsible for mixing fluid at (or at least near) the boundary. However their relative contributions to the modification of the interior fluid has not been quantified.

Mixing at the bottom occurs in stress-driven boundary layers (which result from the no-slip boundary condition) associated with large- or mesoscale currents and with tidal motions. [Armi and D'Asaro \(1980\)](#) observed bottom mixed layers, presumably due to boundary layer turbulence, to persist for many days over the abyssal plain. Bottom flows may be intensified by hydraulic effects. Strong downslope flows have been documented in several (upper ocean) locations ([Wesson and Gregg 1994](#); [Farmer and Armi 1999](#); [Moum and Nash 2000](#); [Nash and Moum 2001](#)). Hydraulically controlled flow through deep ocean gaps in the Mid-Atlantic Ridge may be responsible for the energetic turbulence observed there ([Polzin et al. 1997](#)). The internal tide may also contribute to mixing at the bottom when the bottom slope is near to the tide's characteristic direction. [Thorpe et al. \(1990\)](#) observed that the largest fluctuations in benthic boundary layer structure varied with tidal period in the vicinity of bottom slopes critical to the M_2 internal tide.

In a stratified fluid, internal gravity waves interact with sloping boundaries in various ways ([Thorpe 1999](#) provides a recent review). These interactions can effect mixing both at the boundary and, by generating internal waves that propagate away from the bottom, in stratified fluid away from the boundary. Observations of enhanced mixing as well as enhanced finescale shear and strain several hundreds of meters above the Mid-Atlantic Ridge ([Polzin et al. 1996](#)) and its foothills ([Ledwell et al. 2000](#)) east of the Brazil Basin strongly implicate internal gravity waves in generating turbulence remote from the boundary. Correlation of depth-integrated turbulent dissipation rates and rms tidal currents suggests that tidal flow over the bottom is responsible for energizing the internal wave field above the bottom. High turbulence levels have also been observed over Fieberling Seamount in association with tidally driven vorticity and diurnal shear ([Kunze and Toole 1997](#)) and over its flanks in association with elevated finescale shear and strain in the internal wave band ([Toole et al. 1997](#)). As well, high turbulence levels have been observed along characteristics of the internal tide emanating from topographic variations ([Lueck and Mudge 1997](#); [Lien and Gregg 2001](#)).

Away from the bottom, signatures of bottom mixing exist as intermediate nepheloid layers (INLs), which are local vertical maxima in suspended particulate matter. The existence of INLs supports the suggestion by [Armi \(1978\)](#) that water mixed vertically in bottom boundary layers over sloping bathymetry may detach from the bottom and spread along isopycnals to the interior. The steplike structure caused by intermittently mixed and detached layers would be lost in time by interleaving and gentle interior vertical mixing. These layers have been found away from boundaries ([Pak et al. 1980b](#)) and in deep water off the continental slope ([Thorpe and White 1988](#)).

Direct observations of boundary mixing to date have been made using vertical profilers, which provide excellent vertical resolution of properties in the water column. It is not possible, however, to rapidly deploy such devices in the deep ocean. Tethered profilers ([Moum et al. 1995](#)) are impractical and untethered profilers ([Schmitt et al. 1988](#)) have long turnaround times, and hence slow repetition rates (at most, five profiles per day to 3000 m).


To obtain more intensive measurements of deep boundary mixing we have developed an instrument that can be towed behind a ship (presently to 3400-m depth) for many days at a time. This allows it to remain in the vicinity of the boundary for extended periods.


Reported herein are some results from the first set of observations of boundary mixing using our towed body over a small region of Oregon's continental slope. These observations revealed topographically induced mixing similar in magnitude and vertical structure to that observed by [Ledwell et al. \(2000\)](#) over abyssal hills in the eastern Brazil Basin. The highest values of turbulent dissipation measured and the most extensive regions (~ 5 km) of continuously high dissipation were detected along a bottom slope critical to the M_2 internal tide. Our observations include intermediate nepheloid layers with distinctive water mass properties, representing fluid which has recently been in contact with the bottom, has mixed and detached.

In [section 2](#), we discuss the instrumentation. A description and examples of the data used in this study are given in [section 3](#). Site bathymetry and background currents are presented in [section 4](#). The variability of turbulent kinetic energy dissipation, ϵ , along extended tow paths is described in [section 5](#) and the vertical structure with respect to the bottom in [section 6](#). To support the contention that averages of ϵ (and hence diffusivity, K_ρ) are unaffected by noise, we also present a statistical analysis. Quantification of the vertical structure of K_ρ and the resulting turbulent heat flux ([section 7](#)) permits an estimate of the heat flux divergence immediately above the bottom. An example of a deep intermediate nepheloid layer is found in [section 8](#). Discussion ([section 9](#)) and conclusions ([section 10](#)) follow.

2. Methods

a. Instrumentation

The instrument package, MARLIN, is 5 m long with maximum diameter 0.8 m (Fig. 1 ). Hydrodynamic fairing is provided by an aircraft wing tank. The wing tank houses pressure cases, cables, and flotation. MARLIN weighs 4000 N in air. To minimize hydrodynamic forces on the body, thereby permitting low-noise turbulence measurements (Osborn and Lueck 1985; Lueck 1987; Fleury and Lueck 1991), the body is only slightly heavy in water (about 50 N). No depressor planes are used to keep it down; rather, it is towed behind a heavy body. Dockside static trimming provides an approximate trim, but does not account for dynamic forces that act while underway. MARLIN is finally trimmed to within 2° of horizontal pitch during several test runs at sea.

MARLIN is towed approximately 35 m below a 15-kN streamlined depressor weight from 200 m of Kevlar-reinforced conducting cable (Fig. 2 ). The weight is attached to 9 km of 17.3-mm (standard 0.680 inch) coaxial armoured cable through which power is provided to MARLIN and data transmitted back to the ship. The drag on the body at our typical tow speed of 2 kts (1 m s^{-1}) is less than 90 N, and once the depressor weight has been recovered, MARLIN can be pulled near to the ship by hand for recovery. At the bottom of the 1-m-long fin beneath the hull is a 450 N weight which provides stability to roll. In the case of cable failure, this weight is released via a burn wire triggered by either a pressure switch or a timing circuit (on separate batteries), allowing MARLIN to float.

Turbulence sensors are located at MARLIN's nose, colocated with sensors to measure pressure, temperature, and conductivity. Three airfoil probes sense cross-stream velocity gradient fluctuations (Osborn and Crawford 1980) from which we estimate the rate of dissipation of turbulent kinetic energy, ϵ (Moum et al. 1995). Two probes are aligned to sense downstream gradients of horizontal velocity fluctuations and a third is aligned to sense downstream gradients of vertical velocity fluctuations. A pitot tube senses downstream velocity fluctuations (Moum 1990). Five fast-response thermistors are included in the cluster, two calibrated for full water column temperature response and three set to high gain for targeted temperature ranges (in this way the noise level of the high gain temperature sensors, typically limited by sampling noise, is reduced to $100 \mu\text{K}$). Extra sensors to detect temperature, conductivity and pressure provide redundancy, critical to our objective of running many days continuously.

Ancillary measurements of temperature and conductivity use SeaBird sensors mounted externally on the hull behind the tow point. An impeller flowmeter detects flow speed relative to the body. Upward- and downward-looking 500-kHz SonTek acoustic Doppler current profilers (ADCPs) are deployed along the body. The impeller flow meter frequently fouls and we rely on the ADCP for most flow speed estimates when this occurs.

To detect intermediate nepheloid layers, we mounted an optical backscatter intensity sensor (880-nm light source; Seapoint Sensors) alongside the SeaBird temperature and conductivity sensors.

One of our objectives was to fly MARLIN within 50 m of the bottom. This required a real-time, local measurement of distance to the bottom. A single downward-looking sonar transducer (195 kHz) was mounted on the bottom of the hull forward of the fin. Real-time data processing detects the bottom from the return pulse.


b. Operational considerations

Planning for this experiment required obtaining the best bathymetry available. The National Geophysical Data Center has 150 m (horizontal resolution) bathymetry for the region. However, since we intended to fly MARLIN so close to the bottom, we first steamed along the planned track to obtain local bathymetry using the ship's echosounder. This proved wise, as we discovered one feature several hundred meters high that was not in the bathymetry dataset.

Towing close to the bottom required good communication with the ship's officers. The best mode of operation was to install a real time display of depth on the bridge and to specify a depth and tolerance for the tow. We found that a tolerance of ± 25 m about the specified depth provided MARLIN a reasonable trajectory. Depth tolerance was maintained by slowly adjusting ship speed. The other way to adjust tow depth is to spool cable in or out. This must be done for large depth changes but does not provide as quick a response as changing ship speed.

3. Data

a. Time series

A data record from about 500 m depth over the abyssal plain demonstrates several aspects of the data (Fig. 3 ). During this 320 s record, MARLIN slowed from 108 to 100 cm s^{-1} (due to slowing of the ship) and sank 4 m. Tow speed fluctuations of several centimeters per second on smaller time scales have little influence on the depth of MARLIN. MARLIN

itches with about 0.3° amplitude and rolls less than 0.1° .

The record in [Fig. 3](#) exhibits three distinct sections. Between 30 and 170 s temperature excursions of period ~ 10 s (10 m) are associated with highly intermittent turbulence (as determined by both temperature gradient and shear signals; [Fig. 4](#)). The signature of the temperature ramps suggests shear flow instability in the form of Kelvin–Helmholtz billows. This is indicated by the shape of the along-track temperature gradient, giving nonzero skewness over 8–10 examples of similar (10 m) scale ([Smyth and Moum 2000](#)). Following this (190–270 s) is a continuously turbulent region of about 80 m lateral extent. After 275 s, the temperature record is relatively smooth and both temperature gradient and shear signals are indistinguishable from noise. For much of the data this far from the bottom, turbulence signals were below system noise.

b. Dissipation spectra

Determination of \mathcal{E} from airfoil probe signals, $\partial v/\partial x$, $\partial w/\partial x$, was made by integrating spectra corrected for filter attenuation and the probe's spatial attenuation following [Moum et al. \(1995\)](#).

A spectrum of energetic turbulence is shown in [Fig. 5](#). For comparison are shown spectra computed from simultaneous signals of three orthogonal linear accelerometers and converted to equivalent shear spectra, $\psi^a_{\partial v/\partial x} = \psi_a/U^2$, where U is the measured flow speed past the body. The dominant source of noise is hydrodynamically induced body motions, sensed directly by the airfoil probes. The measured body acceleration, a , contributes a fictitious spatial gradient of velocity to the signal, expressed as a/U . This was estimated by [Moum and Lueck \(1985\)](#) to be the single largest source of noise to dissipation measurements on the CAMEL profiling instruments.

Where the spectrum of a/U , or $\psi^a_{\partial v/\partial x}$ is small relative to that of $\psi_{\partial v/\partial x}$ (as in [Fig. 5](#)) the signal is uncontaminated by hydrodynamically induced vibrations of the body. As $\psi^a_{\partial v/\partial x}$ approaches $\psi_{\partial v/\partial x}$, some portion of the spectrum may be influenced by body accelerations and care must be taken in integrating the spectrum. We have found that the signature of hydrodynamically induced signal contamination changes with tow speed and attitude. An example showing signal slightly above $\psi_{\partial v/\partial x}$ is shown in [Fig. 6](#). The low frequencies of $\psi^a_{\partial v/\partial x}$ represent the component of gravitational acceleration sensed by the accelerometers when the body pitches or rolls (note the smaller low-frequency level in the vertical, or heave, component A_z in [Figs. 5](#), [6](#)). These do not contaminate $\psi_{\partial v/\partial x}$. The example shown in [Fig. 6](#) has an average value (among the three airfoil probes) of $\mathcal{E} \simeq 5 \times 10^{-10} \text{ m}^2 \text{ s}^{-3}$. We believe that no values of \mathcal{E} greater than $7 \times 10^{-10} \text{ m}^2 \text{ s}^{-3}$ are subject to hydrodynamic noise contamination. Real values of \mathcal{E} associated with our estimate of $\mathcal{E} = 7 \times 10^{-10} \text{ m}^2 \text{ s}^{-3}$ are indeterminately smaller.

The spectra resemble the theoretical form of [Panchev and Kesich \(1969\)](#) better than the empirical form of [Nasmyth \(1970\)](#) at frequencies greater than the peak in the dissipation spectra.

4. Background

A set of measurements using MARLIN was made along the continental slope off Oregon in August 1999. Tows were made in the north–south direction at nominally 1 m s^{-1} between 43° and 44°N , each tow taking approximately 1 day. To investigate the importance of topographic interactions with the flow, tows were made along two sections across the toe of a large submarine landslide that extends perpendicularly from the continental slope ([Fig. 7](#)). To assess background levels of turbulence, tows were also made farther offshore, at 1000-m and 1500-m depth above the 3100 m deep abyssal plain.

Currents measured from MARLIN (calculated by differencing ship and MARLIN speeds and lowpass filtering at 2 h) indicate the dominant signal to have a period of 12.42 h (semidiurnal lunar tidal period, M_2) with variable amplitude (peak 0.08 m s^{-1} ; predominantly north–south direction; north–south currents only are plotted in [Fig. 8](#)). These are in approximate agreement with the barotropic tidal predictions from the model of [Egbert \(1997\)](#). Modeled east–west currents are smaller by a factor of 10. Hence, the dominant tidal flow was along the slope but across the toe of the submarine landslide.

5. Variability of \mathcal{E} along the tow paths

Tows ranged in length from 40 to 95 km, totaling more than 800 km. Three tows were made at nominally 1500, 2000, and 2500 m above the 3100 m deep abyssal plain along $125^\circ 36' \text{ W}$ (the lower two of these are depicted in [Fig. 9](#)). Obvious in the plots is the difficulty in maintaining a fixed depth (the tow paths in [Fig. 9](#) are from early in the experiment, while those in [Fig. 10](#) were made toward the end when we had revised our operational procedures). With no active control surface on MARLIN (which would contribute an unacceptable level of hydrodynamically induced noise) and

with a fixed length of tow cable deployed, MARLIN's depth varies solely due to speed fluctuations, which are caused almost entirely by ship speed variations (the largest drag element in the system is the cable, so speed variations cause depth variations via changes in cable drag).

Also obvious in [Fig. 9](#) is that most of the ϵ values are quite low (blue in color; $\epsilon < 1 \times 10^{-9} \text{ m}^2 \text{ s}^{-3}$). Over the 150 km of tow shown here only a single short portion was actively turbulent. This was an event of 200 m lateral extent consisting of a series of temperature ramps that indicate a stratified, and potentially sheared interface.

Tows over the submarine landslide ([a, b](#) in [Fig. 7](#)) indicate that the occurrence of higher values of ϵ increases with proximity to the bottom ([Figs. 10, 11](#)). Here high values of ϵ were observed in regions of horizontal extent several kilometers and greater. The data have been heavily averaged to permit depiction on the page and we can only infer the larger scale nature of the structure from these figures (details apparent in [Figs. 3, 4](#) that offer potential clues to the instability mechanism are not evident in [Figs. 10, 11](#)). Fifteen second (nominally 15 m horizontal) estimates of ϵ occasionally exceeded $10^{-6} \text{ m}^2 \text{ s}^{-3}$ in the continuously turbulent fluid (5 km horizontal extent) immediately above the south end of the landslide at 43.4°N, 125°14 W ([Fig. 11](#)).

6. Vertical structure and statistics of ϵ

Initially, ϵ was computed from 1-s spectral estimates. From these, an integral timescale ([Emery and Thomson 1997](#)) was estimated at roughly 15 s, approximately equivalent to 15 m in the horizontal. Bootstrap confidence intervals shown in [Fig. 12](#) were estimated from the 15 s averaged data. Determination of an integral scale from these data was not very satisfactory. It was done by integrating the autocorrelation from 1 s lag to its zero-crossing ([Poulain and Niiler 1989](#)). Variability was significant from tow to tow, especially between tows near to and away from the bottom. Use of a single value of 15 s, then, is somewhat arbitrary.

A mean vertical profile of ϵ was computed as follows: individual 15 s estimates of ϵ were binned over 100 m of tow track and assigned a mean depth; the bottom depth was estimated by averaging the depths measured by the ship's echosounder. The ϵ estimates were then averaged, independent of horizontal position, in 50 m vertical intervals as a function of height above bottom ([Fig. 12](#)).

The mean profile of ϵ indicates large mean values in the bottom 150 m, but also elevated values (relative to 1000 m to 2000 m above bottom) as high as 600 m above the bottom. Above 600 m, mean values are nearly constant at about $(4-7) \times 10^{-10} \text{ m}^2 \text{ s}^{-3}$.

An important consideration is the effect of noise on our lowest estimates of ϵ . This is complicated by the fact that there is no fixed noise level. The lowest 15 s estimates of ϵ are $5 \times 10^{-11} \text{ m}^2 \text{ s}^{-3}$. However, the vibrational noise of the body varies and higher, contaminated values are part of the distribution in [Fig. 13](#), which shows the population distribution of individual, 1 s estimates of ϵ between 2050 and 2100 m above the bottom. It is the mean value of this distribution that is plotted at that depth in [Fig. 12](#). This distribution exhibits a broad peak about the median value of $2.6 \times 10^{-10} \text{ m}^2 \text{ s}^{-3}$, which is half the mean value.

If the data distribution shown in [Fig. 13](#) is due partly to contaminated signal, at issue is whether the mean value we have computed is significant. In [section 3b](#) it is determined that values of the shear spectrum emerge from the level of hydrodynamic noise when $\epsilon > (3-7) \times 10^{-10} \text{ m}^2 \text{ s}^{-3}$. When ϵ is above that value, its estimation is unaffected by hydrodynamic noise; below that value, its estimation may be affected. To address this, we have performed a series of experiments in which all values smaller than a threshold level (ϵ_{th}) were set to zero and the mean was recomputed ($\langle \epsilon \rangle$).

The result (lower panel of [Fig. 13](#)) is a reduction of the mean by 20% when the lowest 50% of the data (all values $< 3 \times 10^{-10} \text{ m}^2 \text{ s}^{-3}$) were set to zero and by 35% when the lowest 75% ($< 4 \times 10^{-10} \text{ m}^2 \text{ s}^{-3}$) were set to zero. If we set the lowest 90% of the data to zero, the mean changes by a factor of 2. This is a particularly stringent test. We know that a large percentage of the data we have set to zero is uncontaminated and we have no reason to expect background oceanic levels to be zero. The value of ϵ_{th} below which 90% of the data lies is greater than the maximum noise level of $7 \times 10^{-10} \text{ m}^2 \text{ s}^{-3}$ determined from examination of spectra. The value of $\epsilon_{\text{th}} = 7 \times 10^{-10} \text{ m}^2 \text{ s}^{-3}$ is used to compute a minimum value of $\langle \epsilon \rangle$ as a lower bound on our vertical mean profile of ϵ (this is shown in [Fig. 15](#) in relation to the Brazil Basin profiles).


By comparison, the distribution of ϵ near the bottom ([Fig. 14](#)) differs significantly from that 2000 m above ([Fig. 13](#)), reproduced in light shading in [Fig. 14](#).


This analysis demonstrates two points. First, the upper 5%–10% of the ϵ estimates dominate the mean. Second, our detection limit of ϵ is sufficiently low that mean values are unaffected. In part, this is because of the large number of


samples in each population.


7. Turbulent diffusivity and flux

Local vertical profiles of density and temperature were determined from MARLIN's continual depth adjustments. This permitted calculation of vertical gradients, and the local buoyancy frequency $N^2 = -(g/\rho)\partial\rho/\partial z$, where $g = 9.81 \text{ m s}^{-2}$, ρ is density, and z the vertical coordinate). Local estimates of \mathcal{E} and N were made over ascending and descending depth adjustments, and combined to estimate the turbulent diffusion coefficient $K_\rho = \Gamma\mathcal{E}/N^2$; Γ , taken here to be 0.2, is a flux coefficient simply related to a flux Richardson number and is, on average, 0.2 for well-developed turbulence; [Osborn \(1980\)](#), [Moum \(1996\)](#), [Smyth et al. \(2001\)](#).

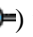
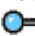
Stratification was significant at all depths ([Fig. 15](#) ). No correlation was found between \mathcal{E} and N^2 , and the lowest individual values of N^2 were not associated with the highest values of \mathcal{E} .

Two thousand meters above the bottom, $K_\rho \cong 2 \times 10^{-5} \text{ m}^2 \text{ s}^{-1}$ ([Fig. 15](#) ), in agreement with thermocline dye release experiments ([Ledwell et al. 1993](#)): K_ρ increased toward the bottom, exceeding $10^{-4} \text{ m}^2 \text{ s}^{-1}$ a few hundred meters above the bottom and approaching $10^{-3} \text{ m}^2 \text{ s}^{-1}$ 50–100 m above the bottom.

Comparison to \mathcal{E} observations made over abyssal hills at bottom depths of 4000–4500 m in the eastern Brazil Basin ([Ledwell et al. 2000](#)) indicates no significant difference when plotted as a function of height above bottom ([Fig. 15](#) ).

The turbulent heat flux $J_q = -\rho C_p K_\rho \theta_z$, (where C_p is the specific heat of seawater, $\sim 4000 \text{ J kg}^{-1} \text{ K}^{-1}$, θ is potential temperature, and θ_z its vertical gradient) indicates an increase from roughly 0.1 W m^{-2} in mid water column to $\sim 2 \text{ W m}^{-2}$ near the bottom ([Fig. 16](#) ). The heat flux divergence indicates a heating from above of the water nearest the bottom.

8. Intermediate nepheloid layers

A common feature of these observations, revealed by our optical backscatter probe, is the presence of INLs of varying intensity and lateral dimension. These are layers of enhanced optical backscatter intensity. At these depths ($>1000 \text{ m}$) the scatterers (dead biological matter or terrigenous matter) represent resuspended sediments ([Pak et al. 1980a,b](#)), indicating bottom origin, following active mixing and subsequent separation from the bottom. INLs were observed in all tows, exhibiting north–south lateral extents of $O(100 \text{ m})$ to $O(10 \text{ km})$. One example which serves to demonstrate a few general characteristics ([Fig. 17](#) ) was observed 600 m above the bottom and more than 10 km from any topography at the layer depth. We do not have comprehensive density surveys to establish isopycnals, but presumably the INL migrated to its observed location along isopycnal surfaces. It was at least 80 m thick. A tow 80 m higher along the same path the previous day failed to detect an INL with the same θ – S properties. CTD profiles made nearby during the cruise establish significant stratification below the depth of this INL and it is inconceivable that this is a local boundary layer 600 m thick. It extended almost 10 km from south to north along the tow. Lateral deviations of MARLIN from its tow path are estimated to be more than 100 m, providing a lower bound on the INL's east–west extent. INL water mass properties (θ and S) distinguish it from surrounding waters ([Fig. 17e](#) ). Examination of σ_θ versus depth profiles reveals that fluid north of the INL is lighter than fluid in the INL at the same depth. Evidence of mixing with waters on the periphery of the INL is provided by the straight lines perpendicular to and joining light and dark distributions in θ – S space. Somewhat elevated values of \mathcal{E} were observed at the periphery of the INL.

9. Discussion

Mean vertical profiles of \mathcal{E} derived from the measurements over the submarine landslide perpendicular to the continental slope off Oregon are not significantly different from those over abyssal hills in the Brazil Basin. This is despite the fact that the respective observations were made not only in different oceans and different depth ranges, but also very different topographies and stratifications, and using different sampling strategies. In each dataset, the profile of \mathcal{E} indicates a vertical decay scale of about 100 m above the bottom.

The value of \mathcal{E} estimated for an internal gravity wave field characterized by the Garrett and Munk model spectrum ([Garrett and Munk 1975](#), hereafter GM) has been calibrated by comparison to internal gravity wave shear levels and measurements of \mathcal{E} in the ocean interior by [Gregg \(1989\)](#) and [Polzin et al. \(1995\)](#). This leads to $\mathcal{E}_{\text{GM}} = 7 \times 10^{-10} \langle N^2/N_o^2 \rangle \text{ m}^2 \text{ s}^{-3}$, where $N_o = 0.0052 \text{ s}^{-1}$. Here we have set the shear to that corresponding to the [GM](#) model spectrum, so that \mathcal{E}_{GM}

is a function of the local stratification only. Estimates of ϵ_{GM} computed from the profiles of N shown in [Fig. 15](#) are

fairly constant at $1 \times 10^{-10} \text{ m}^2 \text{ s}^{-3}$ (as noted in [Fig. 15](#)), or about $5 \times$ smaller than observed values of ϵ above 1000 m. This suggests that interval gravity wave energy levels were enhanced over the open ocean [GM](#) value.

In the Brazil Basin, enhanced ϵ was hypothesized to be caused by vertical propagation of internal gravity waves from a rough bottom associated with tidal currents flowing over the bottom ([Ledwell et al. 2000](#)). While this may be partly true for the Oregon slope, there are also hints of other processes at work. One source for bottom mixing may be the interaction of the tide with topography ([Thorpe et al. 1990](#)). Strong tidal interactions with sloping bottoms are thought to occur at locations where wave particle velocities parallel the slope ([Baines 1974](#)). Indeed, INLs have been observed to form in deep water over the continental slope regularly on M_2 tidal cycles ([Thorpe et al. 1990](#)). For the M_2 internal tide, particle velocities parallel the characteristic

$$\frac{dz}{dx} = \pm \left[\frac{\omega_{M_2}^2 - f^2}{N^2(z) - \omega_{M_2}^2} \right]^{1/2}$$

(f is the local Coriolis frequency and ω_{M_2} is the M_2 tidal frequency). This characteristic was computed from local density profiles measured at the time of the experiment and depicted in [Fig. 18](#) adjacent to the slope at the south edge of the landslide. The most intense and the most extensive region of turbulence was observed along the slope that parallels the M_2 tidal characteristic.

There are several mechanisms that could result in flow instability leading to turbulence (these are reviewed by [Thorpe et al. 1990](#)) due to the incidence of the internal tide on a critical slope. The dynamics of internal wave reflection and associated shear intensification has been studied numerically for simplified bathymetry ([Slinn and Riley 1996](#), for example). For complex topography high-wavenumber internal wave beams may be radiated from the boundary and act as an additional source of shear. Our present observations do not permit us to directly observe the details of this conversion. Diagnosing the specific mechanisms by which the observed turbulence was generated will require further analysis (more measurements and numerical simulations) and will be a focus of future research.

If critical slope interaction of the tide with topography is in part responsible for the detached boundary layers we have observed as INLs, spatial and temporal variations in volume and water mass properties may be quite large. These will depend on the local shape of the topography, variations in $N^2(z)$, and both phase and amplitude of tidal currents. They will also depend on local mesoscale variability, which is presumably responsible for both moving mixed fluid from the boundary and helping to replenish the boundary layer.

The vertical heat flux due to turbulence is almost constant above 1000 m ([Fig. 16](#)). Ignoring the smaller scale variations, the heat flux slowly increases to 250 m above the bottom, below which it rapidly increases. The vertical heat flux in the water column adjacent to the ocean bottom must equal the geothermal heat flux at the ocean bottom, which is of order 0.1 W m^{-2} , acting to heat fluid from below. This means that everywhere above the bottom-most layer and below 1000 m, fluid parcels are cooled as more heat leaves a fluid parcel from below than is input at the top. At the ocean bottom, however, presumably in a bottom boundary layer, fluid parcels are heated from both above and below. Quantitatively, fluid between 250 and 1000 m is cooled at a rate of $\sim 0.1 \text{ W m}^{-2}$, while fluid at the bottom is warmed at a rate of almost 3 W m^{-2} (mostly at the expense of the fluid immediately above, where the largest vertical divergence of the flux is observed). At this rate, the lower 250 m would become unstratified in $O(100 \text{ d})$, assuming $\partial\theta/\partial z = 0.002 \text{ K m}^{-1}$. Of course, this cannot happen for very long and the persistence of such a flux divergence means that fluid at the bottom must be replenished. How is this done?

One mechanism by which fluid at the boundary can be replaced is boundary layer detachment, following the experiments of [Phillips et al. \(1986\)](#). Here an internal pycnocline adjacent to a sloping bottom at which enhanced mixing is generated spreads both up and down the slope. The hydrostatic pressure gradient thus formed drives an upslope flow below the pycnocline and a downslope flow above the pycnocline. The resulting convergent flow in the pycnocline at the slope is relieved by a flow away from the boundary toward the fluid interior. While the bathymetry, stratification and flow in the real ocean are certainly much more complicated than those of the lab studies, perhaps the lab studies offer a working hypothesis that helps to understand at least part of our observations, and suggest avenues for further seagoing experimentation.

If boundary layer detachment, as suggested above, is the key to replenishing fluid at the boundary as required by the divergent heat flux at the boundary, the observed INLs may be its interior signature. It has been suggested ([Armi 1978](#); [Thorpe et al. 1990](#)) that detached and mixed boundary layers that are subsequently stirred along isopycnals could be largely responsible for mixing the ocean's interior. This mechanism has been discounted in recent studies of deep boundary mixing

(Polzin et al. 1996; Lueck and Mudge 1997; Ledwell et al. 2000) in favor of mixing away from the bottom by internal gravity waves that originate at the bottom.

The observed INLs had traveled considerable distances from their origins. We assume that, statistically, these water parcels will continue to be moved toward the ocean interior via mesoscale processes (Armi 1978). As they proceed, particles will continue to settle out, eventually precluding optical detection (hence association with bottom origin), and θ and S anomalies will continue to diffuse at midgyre mixing rates, thereby modifying the water mass structure of the ocean interior. The transport of mixed fluid away from the bottom within detached boundary layers represents a contribution to the larger scale flux of properties which is in addition to that due to mixing of fluid above the bottom by the action of internal gravity waves generated at rough bottoms.

The observation of lateral density gradients between the INL and peripheral waters and higher mixing rates at the edges suggests the possibility of secondary processes that may further enhance the mixing of the INL. We cannot detect a distinct velocity signature of the INL. However, there may be a geostrophic flow along the density front. The prospect of wave-trapping along the front is another issue for future examination.

10. Conclusions

Two important aspects of these observations are new and due to the method of observation. The first is the great lateral extent of fluid that is actively turbulent. The second is the clear identification of a water mass with distinctive θ - S properties and a maximum in suspended particulate matter. This is the signature of fluid that has previously been in contact with the bottom and provides grounds for more intensive investigation of detached boundary layers.

For a nearly constant stratification, enhanced mixing near the bottom implies a vertical flux divergence there. To continue in an averaged sense, this requires sufficient (likely intermittent) replenishment of bottom fluid. A means by which this can be accomplished at a sloping boundary has been indicated in the experiments of Phillips et al. (1986). We have suggested that an intermediate nepheloid layer with characteristics such as we have observed could be a consequence.

The vertical structure of σ above the bottom in these observations is not significantly different from that found above abyssal hills in the Brazil Basin.

These data may reveal the turbulence associated with interactions of the internal tide with a critical slope. The evidence for this is weak, and identification of the exact mechanism is left to further analysis. However, this adds to the observations of Thorpe et al. (1990) that indicate large variations in bottom boundary layer structure at tidal periods in the vicinity of bottom slopes critical to the internal tide.

Acknowledgments

This work was funded by the National Science Foundation. We are grateful to the captain and crew of R/V *Wecoma* for their general help as we developed our deployment and recovery techniques over several engineering cruises. The engineering and construction of MARLIN and its electronic hardware and software was a group effort, and we acknowledge the work of Mike Neeley-Brown, Mike Zelman, Ray Kreth, and Greig Thompson. Gary Egbert kindly provided tidal analyses. We appreciate comments by Eric Kunze, Jody Klymak, and Alexander Perlin on an early version of this paper.

REFERENCES

- Armi L., 1978: Some evidence for boundary mixing in the deep ocean. *J. Geophys. Res.*, **83**, 1971–1979. [Find this article online](#)
- Armi L., and E. D'Asaro, 1980: Flow structures of the benthic ocean. *J. Geophys. Res.*, **85**, 469–484. [Find this article online](#)
- Baines P. G., 1974: The generation of internal tides over steep continental slopes. *Proc. Roy. Soc. Math. Phys. Eng. Sci.*, **277**, 27–58. [Find this article online](#)
- Egbert G. D., 1997: Tidal inversion: Interpolation and inference. *Progress in Oceanography*, Vol. 40, Pergamon, 53–80.
- Emery W. J., and R. E. Thomson, 1997: *Data Analysis Methods in Physical Oceanography*. Pergamon, 634 pp.
- Farmer D. M., and L. Armi, 1999: Stratified flow over topography: The role of small-scale entrainment and mixing in flow reestablishment. *Proc. Roy. Soc. Math. Phys. Eng. Sci.*, **455**, 3221–3258. [Find this article online](#)
- Fleury M., and R. Lueck, 1991: Fluxes across a thermohaline interface. *Deep-Sea Res.*, **38**, 745–769. [Find this article online](#)

- Garrett C., 1993: A stirring tale of mixing. *Nature*, **364**, 670–671. [Find this article online](#)
- Garrett C., and W. H. Munk, 1975: Space–time scales of internal waves: A progress report. *J. Geophys. Res.*, **80**, 291–297. [Find this article online](#)
- Gregg M. C., 1987: Diapycnal mixing in the thermocline: A review. *J. Geophys. Res.*, **92**((C5)), 5249–5286. [Find this article online](#)
- Gregg M. C., 1989: Scaling turbulence dissipation in the thermocline. *J. Geophys. Res.*, **94**((C5)), 9686–9698. [Find this article online](#)
- Kunze E., and T. B. Sanford, 1996: Abyssal mixing: Where it is not. *J. Phys. Oceanogr.*, **26**, 2286–2296. [Find this article online](#)
- Kunze E., and J. M. Toole, 1997: Tidally driven vorticity, diurnal shear and turbulence atop Fieberling Seamount. *J. Phys. Oceanogr.*, **27**, 2663–2693. [Find this article online](#)
- Ledwell J. R., A. J. Watson, and C. S. Law, 1993: Evidence for slow mixing across the pycnocline from an open-ocean tracer-release experiment. *Nature*, **364**, 701–703. [Find this article online](#)
- Ledwell J. R., E. Montgomery, K. Polzin, L. S. Laurent, R. Schmitt, and J. Toole, 2000: Evidence for enhanced mixing over rough topography in the abyssal ocean. *Nature*, **403**, 179–182. [Find this article online](#)
- Lien R.-C., and M. C. Gregg, 2001: Observations of turbulence in a tidal beam and across a coastal ridge. *J. Geophys. Res.*, **106**, 4575–4591. [Find this article online](#)
- Lueck R. G., 1987: Microstructure measurements in a thermohaline staircase. *Deep-Sea Res.*, **34**, 1677–1688. [Find this article online](#)
- Lueck R. G., and T. D. Mudge, 1997: Topographically induced mixing around a shallow seamount. *Science*, **276**, 1831–1833. [Find this article online](#)
- Moum J. N., 1990: Profiler measurements of vertical velocity fluctuations in the ocean. *J. Atmos. Oceanic Technol.*, **7**, 323–333. [Find this article online](#)
- Moum J. N., 1996: Efficiency of mixing in the main thermocline. *J. Geophys. Res.*, **101**((C5)), 12057–12069. [Find this article online](#)
- Moum J. N., and R. G. Lueck, 1985: Causes and implications of noise in oceanic dissipation measurements. *Deep-Sea Res.*, **32**, 379–390. [Find this article online](#)
- Moum J. N., and T. R. Osborn, 1986: Mixing in the main thermocline. *J. Phys. Oceanogr.*, **16**, 1250–1259. [Find this article online](#)
- Moum J. N., and J. D. Nash, 2000: Topographically induced drag and mixing at a small bank on the continental shelf. *J. Phys. Oceanogr.*, **30**, 2049–2054. [Find this article online](#)
- Moum J. N., M. C. Gregg, R. C. Lien, and M. E. Carr, 1995: Comparison of turbulence kinetic energy dissipation rate estimates from two ocean microstructure profilers. *J. Atmos. Oceanic Technol.*, **12**, 346–366. [Find this article online](#)
- Nash J. D., and J. N. Moum, 2001: Internal hydraulic flows over the continental shelf: High drag states over a small bank. *J. Geophys. Res.*, **106**, 4593–4611. [Find this article online](#)
- Nasmyth P., 1970: Oceanic turbulence. Ph.D. thesis, University of British Columbia, 69 pp.
- Osborn T. R., 1980: Estimates of the local rate of vertical diffusion from dissipation measurements. *J. Phys. Oceanogr.*, **10**, 83–89. [Find this article online](#)
- Osborn T. R., and W. R. Crawford, 1980: An airfoil probe for measuring turbulent velocity fluctuations in water. *Air–Sea Interaction: Instruments and Methods*, F. Dobson, L. Hasse, and R. Davis, Eds., Plenum, 369–386.
- Osborn T. R., and R. G. Lueck, 1985: Turbulence measurements from a towed body. *J. Atmos. Oceanic Technol.*, **2**, 517–527. [Find this article online](#)
- Pak H., L. A. Codispoti, and J. R. V. Zaneveld, 1980a: On the intermediate partical maxima associated with oxygen-poor water off western South America. *Deep-Sea Res.*, **27**, 783–797. [Find this article online](#)
- Pak H., J. R. V. Zaneveld, and J. Kitchen, 1980b: Intermediate nepheloid layers observed off Oregon and Washington. *J. Geophys. Res.*, **85**, 6697–6708. [Find this article online](#)
- Panchev S., and D. Kesich, 1969: Energy spectrum of isotropic turbulence at large wavenumbers. *Compt. Rend. Acad. Bulgare Sci.*, **22**, 627–630.

Phillips O. M., J. H. Shyu, and H. Salmun, 1986: An experiment on boundary mixing: Mean circulation and transport rates. *J. Fluid Mech.*, **173**, 473–499. [Find this article online](#)

Polzin K., J. M. Toole, and R. W. Schmitt, 1995: Finescale parameterizations of turbulent dissipation. *J. Phys. Oceanogr.*, **25**, 306–328. [Find this article online](#)

Polzin K., K. Speer, J. M. Toole, and R. W. Schmitt, 1996: Intense mixing of Antarctic bottom water in the equatorial Atlantic. *Nature*, **380**, 54–57. [Find this article online](#)

Polzin K., J. M. Toole, J. R. Ledwell, and R. W. Schmitt, 1997: Spatial variability of turbulent mixing in the abyssal ocean. *Science*, **276**, 93–96. [Find this article online](#)

Poulain P.-M., and P. P. Niiler, 1989: Statistical analysis of the surface circulation in the California current system using satellite-tracked drifters. *J. Phys. Oceanogr.*, **19**, 1588–1599. [Find this article online](#)

Schmitt R. W., J. M. Toole, R. L. Koehler, E. C. Mellinger, and K. W. Doherty, 1988: The development of a fine- and microstructure profiler. *J. Atmos. Oceanic Technol.*, **5**, 484–500. [Find this article online](#)

Slinn D. N., and J. J. Riley, 1996: Turbulent mixing in the oceanic boundary layer caused by internal wave reflection from sloping terrain. *Dyn. Atmos. Oceans*, **24**, 51–62. [Find this article online](#)

Smyth W. D., and J. N. Moum, 2000: Anisotropy of turbulence in stably stratified mixing layers. *Phys. Fluids*, **12**, 1343–1362. [Find this article online](#)

Smyth W. D., and D. R. Caldwell, 2001: The efficiency of mixing in turbulent patches: Inferences from direct simulations and microstructure observations. *J. Phys. Oceanogr.*, **31**, 1969–1992. [Find this article online](#)

Thorpe S. A., 1999: $75 + 25 = 99 \pm 1$, or, some of what we still don't know: Wave groups and boundary processes. *Ahü Hulikoa: Dynamics of Oceanic Internal Gravity Waves*, P. Müller and D. Henderson, Eds., SOEST Special Publication, 129–135.

Thorpe S. A., and M. White, 1988: A deep intermediate nepheloid layer. *Deep-Sea Res.*, **35**, 1665–1671. [Find this article online](#)

Thorpe S. A., P. Hall, and M. White, 1990: The variability of mixing at the continental slope. *Proc. Roy. Soc. Math. Phys. Eng. Sci.*, **A331**, 183–194. [Find this article online](#)

Toole J. M., K. L. Polzin, and R. W. Schmitt, 1994: Estimates of diapycnal mixing in the abyssal ocean. *Science*, **264**, 1120–1123. [Find this article online](#)

Toole J. M., R. W. Schmitt, K. L. Polzin, and E. Kunze, 1997: Near-boundary mixing above the flanks of a midlatitude seamount. *J. Geophys. Res.*, **102**((C1)), 947–959. [Find this article online](#)

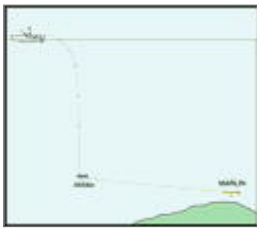
Wesson J. C., and M. C. Gregg, 1994: Mixing at Camarinal Sill in the Strait of Gibraltar. *J. Geophys. Res.*, **99**((C5)), 9847–9878. [Find this article online](#)

Figures



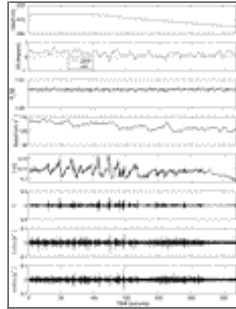
[Click on thumbnail for full-sized image.](#)

FIG. 1. MARLIN suspended from the ship's crane over the side of R/V *Wecoma*. Four tag lines are attached to body hoops and another (foreground) to the crane's headache ball. Locations of sensors discussed in the text are indicated. The obstacle avoidance sonar is flush with the hull



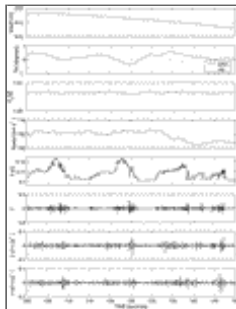
Click on thumbnail for full-sized image.

FIG. 2. Schematic (not to scale) showing deep sea deployment of MARLIN. Research fleet standard 0.680" coaxial cable (9000 m) is terminated at a 15-kN depressor weight. The Kevlar-reinforced conducting tow cable that runs from weight to MARLIN is 200 m long. MARLIN is about 35 m below the depressor weight



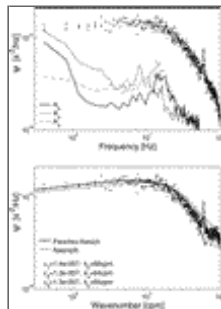
Click on thumbnail for full-sized image.

FIG. 3. Time series of data from MARLIN obtained at depth about 500 m over an abyssal plain 3100 m deep. The length of this record is 320 s (equivalent to about 320 m at our nominal tow speed of 1 m s^{-1} ; fourth panel). The topmost panel shows depth as determined from a pressure measurement and filtered at 2 s. The second panel shows body pitch and roll as determined from linear accelerometers. The third panel indicates vertical acceleration. This is a quiet record. Large values or spikes in A_z contaminate the turbulence signals and are used as a processing filter. Flow speed relative to MARLIN is shown in the fourth panel. Temperature is shown in the fifth panel and its derivative below. The bottom panels depict the signals from two (of three) airfoil probes.



Click on thumbnail for full-sized image.

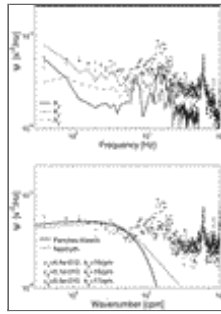
FIG. 4. Expanded view of data from [Fig. 3](#) with the same format.



Click on thumbnail for full-sized image.

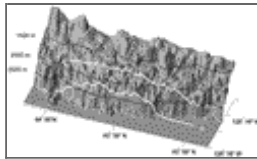
FIG. 5. Spectra of shear from three airfoil probes on MARLIN. The cross (\mathcal{E}_1) and diamond (\mathcal{E}_2) are horizontal components and the box (\mathcal{E}_3) is the vertical component. These spectra were computed from a 12-s record of relatively homogeneous signal. Spectra of acceleration divided by flow speed are also shown; A_x represents along-axis, A_y cross-axis, and A_z vertical components of acceleration. Corrections for probe spatial attenuation and for the anti-aliasing filters have been applied to spectra shown in the lower panel. The turbulent dissipation rates and Kolmogoroff scales (k_η) obtained by integrating corrected spectra

are also shown in the lower panel. For comparison are plotted the empirical spectrum of Nasmyth and the theoretical spectrum of Panchev and Kesich.



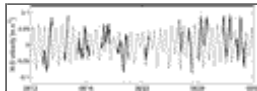
[Click on thumbnail for full-sized image.](#)

FIG. 6. Spectra of shear for a portion of the record in which the signals from the airfoil probes are near their noise level. Format same as [Fig. 5](#)



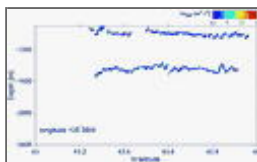
[Click on thumbnail for full-sized image.](#)

FIG. 7. Bathymetry of a large submarine landslide off Oregon's continental slope. Isobaths (1500, 2000, 2500 m) are denoted by thin black lines. White lines indicate the bathymetry immediately below sequences of MARLIN tows. The minimum depth of the offshore track (a) is 2025 m and that of the inshore track (b) 1610 m. The vertical scale is greatly exaggerated. Maximum bottom slopes are less than 1:10



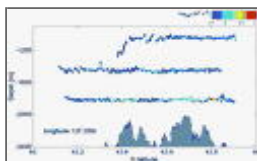
[Click on thumbnail for full-sized image.](#)

FIG. 8. North-south currents measured from ADPs on MARLIN (thick line). To obtain currents from MARLIN, the ship speed was removed from the speed measurement at MARLIN and the result was then lowpass-filtered at 2 h. Barotropic tidal predictions from Egbert's tidal model (thin line) are shown for the same time and location (since the change in phase and amplitude of the predicted currents is small over the 100-km MARLIN track we have considered the track as a single point so far as the barotropic tidal currents are concerned)



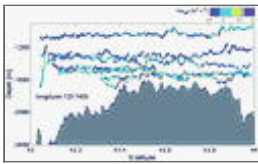
[Click on thumbnail for full-sized image.](#)

FIG. 9. Two MARLIN tows along $125^{\circ}36'$ W over the abyssal plain (depth 3100 m). The depth-latitude track of MARLIN is represented by the lines. The upper tow was made at roughly 1100 m depth, or 2000 m above the bottom. The color of the line indicates the magnitude of $\log_{10}E$, as quantified by the color bar



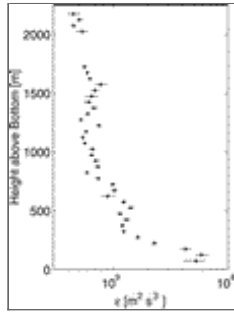
[Click on thumbnail for full-sized image.](#)

FIG. 10. MARLIN tows at $125^{\circ}20'$ W over the submarine landslide (track a in [Fig. 7](#)). The bottom representation shown here is derived from a combination of ship's 12-kHz echosounder and MARLIN's 195-kHz obstacle avoidance sonar



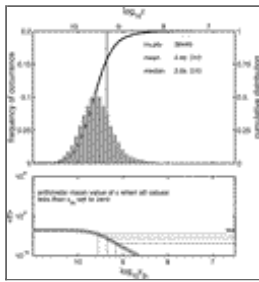
Click on thumbnail for full-sized image.

FIG. 11. MARLIN tows at 125°14' W over the submarine landslide (track **b** in [Fig. 7](#))



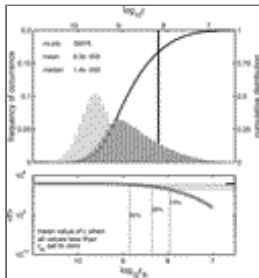
Click on thumbnail for full-sized image.

FIG. 12. Vertical profile of ϵ as a function of height above the bottom: 95% bootstrap confidence intervals of the mean values computed from 15-s time averages (the integral timescale estimate) are plotted for each data point



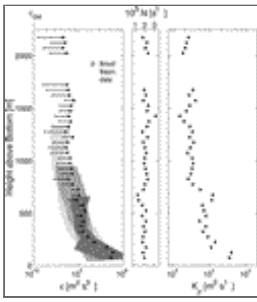
Click on thumbnail for full-sized image.

FIG. 13. Statistics of ϵ for all of the data obtained between 2050 and 2100 m above the bottom. The mean value is that shown in [Fig. 12](#). The upper panel displays population and cumulative distributions. The vertical line represents the mean, and its thickness the 95% bootstrap confidence intervals on the mean. The lower panel represents the results of an experiment in which all the samples smaller than a threshold value, ϵ_{th} , are replaced by zero and the mean value of the population, $\langle \epsilon \rangle$, recomputed. The thin lines indicate the value of $\langle \epsilon \rangle$ when the smallest 50%, 75%, and 90% samples are set to zero. The horizontal bar on the right axis represents the sample mean, as in the upper panel



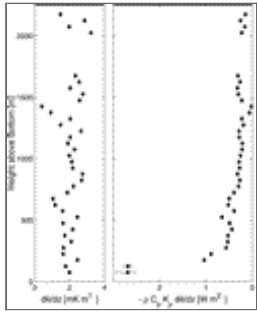
Click on thumbnail for full-sized image.

FIG. 14. Statistics of ϵ for all of the data obtained between 100 and 150 m above the bottom. For comparison, the light gray distribution is reproduced from [Fig. 13](#)



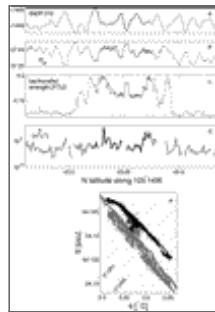
Click on thumbnail for full-sized image.

FIG. 15. Turbulent dissipation, buoyancy frequency, and eddy diffusivity vs height above bottom. In the left hand panel, shaded profiles represent 95% confidence limits of results from the Brazil Basin (Ledwell et al. 2000; light: valley; darker: crest; darkest: slope). Diamonds represent population means of the Oregon slope data computed as described in the text. The lower limit of \mathcal{E} is the lower of either the mean value computed after setting all values $< 7 \times 10^{-10} \text{ m}^2 \text{ s}^{-3}$ to zero (vertical bar), or the lower 95% bootstrap confidence limit shown in Fig. 12 (solid line, no vertical bar). The upper limit is the 95% bootstrap confidence limit from Fig. 12. For higher values of \mathcal{E} , the vertical bar merges with the mean. The estimated value of \mathcal{E} for an open ocean GM internal wave field, as described in the text, is denoted \mathcal{E}_{GM}



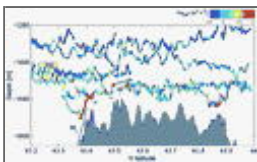
Click on thumbnail for full-sized image.

FIG. 16. Averaged temperature gradient and vertical heat flux due to turbulent mixing vs height above bottom. Upward heat flux is >0



Click on thumbnail for full-sized image.

FIG. 17. Depth (a), potential density σ_θ (b), backscatter strength in Formazin turbidity units (FTU) (c), and \mathcal{E} (120-s averages) (d) along a section of a tow exhibiting a distinct INL [denoted by higher levels of backscatter strength between 43.2° and 43.3°N in (c)]. The unique water mass properties of the INL are distinguished by θ and S (e). Dark represents INL water with θ - S distinct from its periphery



Click on thumbnail for full-sized image.

FIG. 18. Expanded view of Fig. 10, showing the location of the intermediate nepheloid layer discussed in the text (labeled INL) and a characteristic of the M_2 internal tide

top ▲



© 2008 American Meteorological Society [Privacy Policy and Disclaimer](#)

Headquarters: 45 Beacon Street Boston, MA 02108-3693

DC Office: 1120 G Street, NW, Suite 800 Washington DC, 20005-3826

amsinfo@ametsoc.org Phone: 617-227-2425 Fax: 617-742-8718

[Allen Press, Inc.](#) assists in the online publication of *AMS* journals.